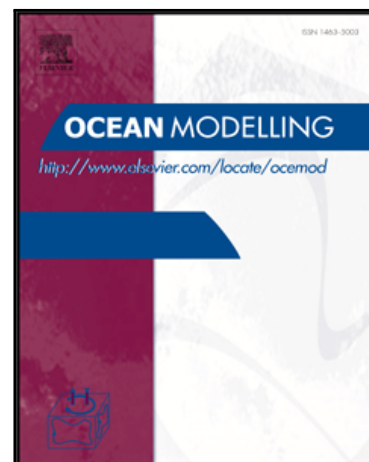


## Accepted Manuscript

The Impact of Atmospheric Storminess on the Sensitivity of Southern Ocean Circulation to Wind Stress Changes

D.R. Munday, X. Zhai

PII: S1463-5003(17)30067-7  
DOI: [10.1016/j.ocemod.2017.05.005](https://doi.org/10.1016/j.ocemod.2017.05.005)  
Reference: OCEMOD 1208



To appear in: *Ocean Modelling*

Received date: 27 February 2017  
Revised date: 4 May 2017  
Accepted date: 13 May 2017

Please cite this article as: D.R. Munday, X. Zhai, The Impact of Atmospheric Storminess on the Sensitivity of Southern Ocean Circulation to Wind Stress Changes, *Ocean Modelling* (2017), doi: [10.1016/j.ocemod.2017.05.005](https://doi.org/10.1016/j.ocemod.2017.05.005)

This is a PDF file of an unedited manuscript that has been accepted for publication. As a service to our customers we are providing this early version of the manuscript. The manuscript will undergo copyediting, typesetting, and review of the resulting proof before it is published in its final form. Please note that during the production process errors may be discovered which could affect the content, and all legal disclaimers that apply to the journal pertain.

**Highlights**

- Increased wind stress can be caused by increased mean atmospheric wind or increased variability of the atmospheric wind.
- The impact of atmospheric wind variability is tested in an idealised Southern Ocean channel model.
- Overturning circulation is more sensitive to wind stress changes when the stress is altered due to changes in variability.
- Increase in sensitivity tied to changes in near-surface dissipation and the dissipation mechanism for kinetic energy.

# The Impact of Atmospheric Storminess on the Sensitivity of Southern Ocean Circulation to Wind Stress Changes

D.R. Munday<sup>a,b,\*</sup>, X. Zhai<sup>c,d</sup>

<sup>a</sup>*British Antarctic Survey, High Cross, Madingley Road, Cambridge, CB30 0ET, UK*

<sup>b</sup>*Atmospheric, Oceanic and Planetary Physics, Department of Physics, University of Oxford, Oxford, OX1 3PU, UK*

<sup>c</sup>*School of Environmental Sciences, University of East Anglia, Norwich, UK.*

<sup>d</sup>*School of Marine Science, Nanjing University of Information Science and Technology, Nanjing, China.*

---

## Abstract

The influence of changing the mean wind stress felt by the ocean through alteration of the variability of the atmospheric wind, as opposed to the mean atmospheric wind, on Southern Ocean circulation is investigated using an idealised channel model. Strongly varying atmospheric wind is found to increase the (parameterised) near-surface viscous and diffusive mixing. Analysis of the kinetic energy budget indicates a change in the main energy dissipation mechanism. For constant wind stress, dissipation of the power input by surface wind work is always dominated by bottom kinetic energy dissipation. However, with time-varying atmospheric wind, near surface viscous dissipation of kinetic energy becomes increasingly important as mean wind stress increases. This increased vertical diffusivity leads to thicker mixed layers and

---

\*Corresponding author

Email addresses: [danday@bas.ac.uk](mailto:danday@bas.ac.uk) (D.R. Munday), [xiaoming.zhai@uea.ac.uk](mailto:xiaoming.zhai@uea.ac.uk) (X. Zhai)

higher sensitivity of the residual circulation to increasing wind stress, when compared to equivalent experiments with the same wind stress held constant in time. This may have implications for Southern Ocean circulation in different climate change scenarios should the variability of the atmospheric wind change rather than the mean atmospheric wind.

*Keywords:* Ocean modelling, Eddy-resolving, Eddy kinetic energy, Surface wind stress, Residual overturning, Near-surface mixing

---

## 1. Introduction

The Southern Ocean (SO) is believed to have a strong influence on global climate via its Residual Meridional Overturning Circulation (RMOC) and the Antarctic Circumpolar Current (ACC) (Meredith et al., 2011). These lead to the upwelling of deep water masses and a zonal connection between major ocean basins, respectively. The Southern Ocean is subject to strong atmospheric winds and makes a large regional contribution to the global integral of mechanical power input to the ocean due to the combination of large zonal wind stress and strong zonal ocean currents (Wunsch, 1998).

Mesoscale eddies play a prominent role in the momentum budget of the Southern Ocean (Munk and Palmén, 1951; Johnson and Bryden, 1989). They flux a large amount of heat southwards (Bryden, 1979; Jayne and Marotzke, 2002; Meijers et al., 2007) and dominate the dissipation of kinetic energy at the bottom of the water column (Cessi et al., 2006; Cessi, 2008; Abernathey et al., 2011). The use of eddy-resolving, or at least eddy-permitting, numerical models allows the emergence of two dynamical phenomena that have been dubbed eddy saturation and eddy compensation.

18 Eddy saturation refers to the loss of sensitivity of the volume transport of  
 19 a circumpolar current to changes in wind stress (Hallberg and Gnanadesikan,  
 20 2006; Tansley and Marshall, 2001). This loss of sensitivity can extend to the  
 21 limit of no zonal wind stress (Munday et al., 2013) and changes in the sensi-  
 22 tivity can be linked to the zonal momentum balance of the current (Munday  
 23 et al., 2015). The degree of eddy saturation that a given model configuration  
 24 achieves is subject to subtleties due, for example, to the inclusion of shallow  
 25 coastal areas (Hogg and Munday, 2014) or the structure of the wind forcing  
 26 (Nadeau and Straub, 2009, 2012).

27 Eddy compensation is the reduced sensitivity to changes in wind stress of  
 28 the RMOC when eddies are resolved or permitted (Viebahn and Eden, 2010;  
 29 Abernathey et al., 2011). Although complimentary to eddy saturation, eddy  
 30 compensation is dynamically distinct (Meredith et al., 2012; Morrison and  
 31 Hogg, 2013). Like eddy saturation, the degree to which a particular model's  
 32 RMOC is compensated depends on several different aspects of the model  
 33 including, but not limited to, whether the surface buoyancy forcing is fixed  
 34 flux vs. restoring to a fixed buoyancy (Abernathey et al., 2011, henceforth  
 35 AMF11) and even the particular timescale used in the restoring condition  
 36 (Zhai and Munday, 2014, henceforth ZM14).

37 Investigations into eddy saturation and eddy compensation using numer-  
 38 ical models typically involve varying the magnitude of the mean wind stress  
 39 in the Southern Ocean, without concern as to whether this variation is due  
 40 to changes in the mean atmospheric wind or atmospheric variability. In prac-  
 41 tice, changes of the mean stress may be brought about by either, owing to  
 42 the nonlinear dependence of the wind stress on the wind (Zhai, 2013). This is

illustrated in Fig. 1a, which shows the mean zonal wind (blue line) from the National Centers for Environmental Prediction (NCEP) reanalysis (Kalnay et al., 1996) as well as the square root of the Eddy Kinetic Energy (EKE) of the atmospheric wind (red line). Clearly the variability of the wind is significant at every latitude, with particularly large values in the Southern Ocean. In Fig. 1b we show the time-mean wind stress (blue line), which includes data from every timestep of the reanalysis, and the wind stress calculated from the mean wind alone using the bulk formula of Large and Pond (1981) (red line). This highlights how variability of the atmospheric wind makes a large contribution to the mean wind stress felt by the ocean, particularly at mid and high latitudes (Zhai, 2013).

[Figure 1 about here.]

Variability of the atmospheric wind results in time-varying wind stress, which is capable of exciting near-inertial motions in the surface ocean. Recent studies (Furuichi et al., 2008; Zhai et al., 2009; Rath et al., 2014) show that the majority of the wind energy input to the near-inertial motions is dissipated and lost to turbulent mixing within the upper 200 m, contributing to deepening of the mixed layer and cooling of the sea surface temperature. Jouanno et al. (2016) demonstrate that the passage of storms over an idealised Southern Ocean leads to a slight enhancement of both mean and eddy kinetic energy. Energy dissipation at depth is also increased, in part due to the generation of more near-inertial waves. In their experiments with storms, there is a shift in the energy balance such that more energy is dissipated by vertical viscous processes with respect to a stormless control experiment.

67 This enhanced dissipation is found to be sensitive to the strength of the wind  
 68 stress and the propagation speed and strength of the storms, with increases  
 69 in any of these leading to further enhancement of the viscous dissipation.

70 Turbulent mixing associated with energy dissipation is also likely to con-  
 71 tribute to water mass transformation processes in the surface diabatic layer.  
 72 Wind stress variability can play a direct role in mode water formation via the  
 73 destruction or creation of potential vorticity at ocean fronts (Thomas, 2005)  
 74 or by generating wave-induced vertical mixing (Shu et al., 2011). Changes  
 75 in the mode of variability of atmospheric wind, i.e. ENSO or the Southern  
 76 Annular Mode, has been observed to change the dominant creation mecha-  
 77 nism for Subantarctic Mode Water (Naveira Garabato et al., 2009). In other  
 78 words, there may be a role for wind-induced near-inertial energy and/or wind  
 79 variability to play in the emergence of eddy saturation and compensation due  
 80 to changes in the mode and intensity of near surface dissipation.

81 In this paper we aim to investigate how changing the wind stress felt by  
 82 the ocean via an increase in the variability of the atmospheric wind, instead  
 83 of the mean wind, impacts upon eddy saturation and eddy compensation. In  
 84 Section 2 we give a brief description of the experimental design and model  
 85 domain. Section 3 describes the circulation achieved at the control wind  
 86 stress. Section 4 discusses the sensitivity to wind stress of the model's energy  
 87 budget under conditions of varying wind. Section 5 discusses the sensitivity  
 88 of the Southern Ocean circulation to wind stress changes. We close with a  
 89 summary and discussion of our results in Section 6.

## 90 2. Experimental Design

91 In order to investigate the impact of time-varying atmospheric wind  
 92 on Southern Ocean dynamics we adopt the idealised MIT general circula-  
 93 tion model (MITgcm, see Marshall et al., 1997a,b) configuration of AMF11,  
 94 adapted to a coarser grid spacing by ZM14 and used by Munday and Zhai  
 95 (2015, henceforth MZ15) to investigate the role of relative wind stress, in  
 96 which the effect of ocean current speed on surface wind stress is taken into  
 97 account, on Southern Ocean circulation. The model domain is a zonally re-  
 98 entrant channel that is 1000km in zonal extent, nearly 2000km in meridional  
 99 extent, and 2985m deep with a flat bottom. There are 33 geopotential lev-  
 100 els whose thickness increase with depth, ranging from 10m at the surface to  
 101 250m for the bottom-most level.

102 The horizontal grid spacing is chosen to be 10km, which is sufficiently fine  
 103 so as to permit a vigorous eddy field without incurring undue computational  
 104 cost. Strictly speaking, this grid spacing makes the model eddy-permitting,  
 105 rather than eddy-resolving, since it does not resolve the first baroclinic defor-  
 106 mation radius throughout the model domain. In particular, it cannot resolve  
 107 the eddy formation process. However, when mature, i.e. at their maximum  
 108 size/strength, eddies are typically several deformation radius across. Fur-  
 109 thermore, this grid spacing is fine enough that substantial eddy saturation  
 110 of the zonal transport occurs in domains with bottom bathymetry (Munday  
 111 et al., 2015). As such, we deem it sufficient for our purposes.

112 [Table 1 about here.]

113 We employ the K-profile parameterisation (KPP) vertical mixing scheme



(Large et al., 1994) and a linear bottom friction. The equation of state is linear and only temperature variations are considered. The model is set on a  $\beta$ -plane. Parameter values for bottom friction, viscosity, etc, are as given in Table 1. The schematic in Fig. 2 indicates the meridional cross-section of the model configuration and forcing, including the northern boundary sponge (see below for details).

[Figure 2 about here.]

The model's potential temperature,  $\theta$ , is forced by a constant heat flux at the surface and restored to a prescribed stratification in a sponge layer within 100km of the northern boundary. The surface heat flux is given by

$$Q(y) = \begin{cases} -Q_0 \sin(3\pi y/L_y), & \text{for } y < L_y/3 \\ 0, & \text{for } y > L_y/3 \end{cases} \quad (1)$$

where  $Q_0$  is the magnitude of the flux and  $L_y$  is the meridional extent of the domain, as per AMF11 and ZM14, with  $y = 0$ km placed at the centre of the domain following MZ15. This broadly describes the observed distribution of surface buoyancy flux around the SO (see Fig. 1 of AMF11). Within 100km of the northern boundary, potential temperature is restored to the stratification given by

$$\theta_N(z) = \Delta\theta (e^{z/h_e} - e^{-H/h_e}) / (1 - e^{-H/h_e}). \quad (2)$$

This describes exponential decay with depth from a surface temperature given by  $\Delta\theta$  to 0 at depth  $-H$  (the total depth of the domain) with an

134  $e$ -folding scale height of  $h_e$ . The restoring time scale for the sponge varies  
 135 from  $\infty$  (no restoring) at the southern edge of the sponge to 7 days at the  
 136 northern edge of the domain. The sponge restoring profile and surface heat  
 137 flux are as shown in Figs. 3a and 3b, respectively.

138 [Figure 3 about here.]

139 In contrast to AMF11 and ZM14, we do not prescribe the wind stress in  
 140 all of our experiments. Instead we prescribe 10m atmospheric wind velocity  
 141 and use the bulk formulae of Large and Pond (1981) to calculate the wind  
 142 stress. These formulae use arguments based on vertical turbulent transport to  
 143 represent the transfer of momentum between the atmosphere and the ocean  
 144 as a stress. MZ15 use so-called relative wind stress, which applies the most  
 145 physically complete bulk formula given by

$$146 \quad \boldsymbol{\tau}_{relative} = \rho_a c_d |\mathbf{U}_{10} - \mathbf{u}_s| (\mathbf{U}_{10} - \mathbf{u}_s), \quad (3)$$

147 where  $\mathbf{U}_{10} = (U_{10}, V_{10})$  is the 10m (atmospheric) wind velocity,  $\mathbf{u}_s = (u_s, v_s)$   
 148 is the surface ocean velocity,  $\rho_a$  is air density, and  $c_d$  is a drag coefficient,  
 149 which itself is a weak function of  $\mathbf{U}_{10} - \mathbf{u}_s$ .

150 MZ15 found that the use of relative wind stress had little effect on the  
 151 sensitivity of the SO RMOG to wind stress and that eddy saturation still  
 152 emerged. In addition, initial experiments combining variable atmospheric  
 153 winds with the relative wind stress formulation indicated that, in this partic-  
 154 ular model domain, the impact of relative wind stress was swamped by the  
 155 time-varying winds. Therefore, in the interests of clarity, we choose to ne-  
 156 glect the surface ocean currents in the calculation of wind stress and instead

157 use the resting ocean approximation. In this limit, the wind stress is given  
158 by

$$159 \quad \boldsymbol{\tau} = \rho_a c_d |\mathbf{U}_{10}| \mathbf{U}_{10}. \quad (4)$$

160 Further, we split the wind into a mean component,  $\bar{\mathbf{U}}_{10}$ , and a perturbation,  
161  $\mathbf{U}'_{10}$ , such that  $\mathbf{U}_{10} = \bar{\mathbf{U}}_{10} + \mathbf{U}'_{10}$ , allowing us to write

$$162 \quad \boldsymbol{\tau} = \rho_a c_d |\bar{\mathbf{U}}_{10} + \mathbf{U}'_{10}| (\bar{\mathbf{U}}_{10} + \mathbf{U}'_{10}). \quad (5)$$

163 In our experiments, the mean 10m atmospheric wind velocity,  $\bar{\mathbf{U}}_{10}$ , is  
164 given by

$$165 \quad \bar{\mathbf{U}}_{10} = \mathbf{U}_0 \cos(\pi y / L_y), \quad (6)$$

166 where  $\mathbf{U}_0 = (U_x, U_y)$  is the peak wind velocity in the zonal and meridional  
167 direction. This is the same profile of mean wind as used by MZ15. In  
168 contrast to MZ15, we specify  $U_x = 7\text{ms}^{-1}$  and  $U_y = 0\text{ms}^{-1}$  and vary  $\mathbf{U}'_{10}$   
169 with pseudo-random perturbations to change  $\boldsymbol{\tau}$ , instead of increasing  $U_x$ .

170 In our first set of experiments, referred to as the stochastic wind exper-  
171 iments, additive white Gaussian noise is used to perturb the wind profile  
172 given by Eq. (6). Every six hours a pseudo-random number from a stan-  
173 dard normal distribution is generated using the polar algorithm attributed  
174 to Marsaglia and Bray (1964). Each experiment uses the same sequence of  
175 pseudo-random numbers, which does not repeat over the life of the experi-  
176 ments.

177 To generate the wind perturbation, the sequence of pseudo-random num-  
178 bers is multiplied by the desired standard deviation of the wind speed,  $\sigma_\tau$ .  
179 The wind profile of Eq. (6) is then uniformly adjusted by this amount, e.g.

180 if a perturbation of  $3.21\text{ms}^{-1}$  is generated, the peak zonal wind would be  
 181  $10.21\text{ms}^{-1}$  and the minimum wind at the northern and southern boundary  
 182 would be  $3.21\text{ms}^{-1}$ . This is illustrated in Fig. 3c by the grey shading, which  
 183 shows the wind profile for one standard deviation of  $9\text{ms}^{-1}$  to either side of  
 184 the mean zonal wind profile given by Eq. (6).

185 We use values of  $\sigma_\tau$  of 0, 3, 6, 9, 12, 15, 18 and  $21\text{ms}^{-1}$ . The experi-  
 186 ment with a standard deviation of  $9\text{ms}^{-1}$  is chosen as the control since this  
 187 matches the roughly constant standard deviation of the NCEP winds over  
 188 the Southern Ocean, as shown in Fig. 1a. This value of  $\sigma_\tau$  gives a peak mean  
 189 wind stress of  $0.17\text{Nm}^{-2}$ , which is close to the mean NCEP wind stress in  
 190 Fig. 1b (blue line) and the control experiments of AMF11, ZM14 and MZ15.  
 191 The mean wind stress that results for  $\sigma_\tau = 0, 9$ , and  $21\text{ms}^{-1}$  are shown in  
 192 Fig. 3d. The peak wind stress that results from the different values of  $\sigma_\tau$  are  
 193 shown in Fig. 4 with the control experiment highlighted using a hexagram.  
 194 The resulting relationship is roughly quadratic, as one would from Eq. (4),  
 195 with a weak cubic term due to  $c_d$  also varying weakly with  $\mathbf{U}_{10}$ .

196 [Figure 4 about here.]

197 The second set of experiments are forced by 50-year averages of the wind  
 198 stress from the stochastic wind experiments. These will be referred to as  
 199 the equivalent stress experiments. By diagnosing the wind stress from the  
 200 stochastic wind experiments we ensure the same pattern of mean wind stress.  
 201 However, because these experiments use a constant pattern of wind stress  
 202 they are effectively changing  $\bar{\mathbf{U}}_{10}$ , instead of  $\mathbf{U}'_{10}$ , to alter the mean wind  
 203 stress. This is expected to have a different impact upon the near-inertial

204 wave field and other near surface mixing processes, and thus may impact  
205 upon the sensitivity of the circumpolar transport and meridional overturning  
206 to changes in wind stress.

207 The stochastic wind experiments are begun from the end of the 800 year  
208 statistically steady control experiment of ZM14. The experiments have the  
209 wind stress used by ZM14 replaced with the zonal wind as described above  
210 and are run for a further 400 years. At the end of this second phase of spin  
211 up we take a 50 year average of the zonal wind stress and use this to drive the  
212 equivalent wind stress experiments. Both the stochastic and equivalent wind  
213 stress experiments are then run to statistical equilibrium. All our results  
214 are drawn from a final 50 year diagnostic phase in which long-term averages  
215 are made. There is a slight discrepancy in the peak wind stress for this  
216 diagnostic run between the stochastic wind experiments and the equivalent  
217 stress experiments. This is due to the pseudo-random nature of the wind  
218 perturbations for the stochastic wind stress experiments, which are only an  
219 approximation to a true normal distribution, and the finite length of the  
220 diagnostic run. This discrepancy is  $< 0.5\%$  for the control experiments and  
221  $\sim 1.5\%$  for the extremes.

222 [Table 2 about here.]

### 223 3. The Control State

#### 224 3.1. Zonal Circulation of the Control State

225 Due to the flat bottomed nature of the model domain, the time-average  
226 flow is zonally-symmetric with time-mean streamlines and temperature con-  
227 tours running east-west. This is much the same as in AMF11, ZM14 and

228 MZ15. Nevertheless, instantaneously a vigorous mesoscale eddy field is  
 229 present resulting in complex non-zonal streamlines and temperature con-  
 230 tours. EKE is likewise zonally symmetric with higher values towards the cen-  
 231 tre of the channel and close to the surface. In both control experiments, peak  
 232 values of EKE at the surface exceed  $0.05\text{m}^2\text{s}^{-1}$ , which is typical in observed  
 233 estimates and high resolution models (see, e.g., Delworth et al., 2012). How-  
 234 ever, the zonal-mean EKE values are somewhat elevated due to the strong  
 235 zonal symmetry and lack of EKE localisation by bottom bathymetry. This  
 236 tends to give high values throughout the channel.

237 Following MZ15 and Munday et al. (2015), we decompose the total cir-  
 238 cumpolar transport,  $T_{ACC}$ , into the bottom transport,  $T_b$ , and the thermal  
 239 wind transport,  $T_{tw}$ , such that  $T_{ACC} = T_b + T_{tw}$ . The bottom transport  
 240 is simply the flow in the bottom model level integrated over the full cross-  
 241 sectional area of the channel. The thermal wind transport is then calculated  
 242 as the residual of  $T_{ACC}$  and  $T_b$  and is what would be obtained from using the  
 243 temperature field in a thermal wind shear calculation.

244 The total circumpolar transport of the stochastic wind stress control,  
 245 with a peak wind stress of  $0.17\text{Nm}^{-2}$ , is  $621\text{Sv}$ . Of this  $542\text{Sv}$  resides in  $T_b$   
 246 and  $78\text{Sv}$  in  $T_{tw}$ . The circumpolar transport for the equivalent stress control  
 247 experiment varies slightly from the stochastic control (see Table 2), with a  
 248  $T_b$  of  $548\text{Sv}$  and a  $T_{tw}$  of  $82\text{Sv}$ . This is due to the slight discrepancy in the  
 249 wind stress, noted in Section 2, and differences in isopycnal slope between  
 250 the two control experiments.

251 The very large  $T_b$  of both control experiments is a consequence of the  
 252 momentum balance in a flat bottomed channel, which leads to the bottom

253 flow accelerating until surface momentum input from the wind is balanced  
 254 by bottom friction (see, e.g., Gill and Bryan, 1971; Bryan and Cox, 1972).  
 255 The approximate momentum balance of the channel can be written as

$$256 \quad \frac{\langle \bar{\tau}_x \rangle}{\rho_0} \approx r_b \langle \bar{u}_b \rangle, \quad (7)$$

257 where  $\langle \bar{\tau}_x \rangle$  is the time and zonal average of the zonal wind stress,  $\langle \bar{u}_b \rangle$  is  
 258 the time and zonal average zonal velocity in the bottom level of the model,  
 259  $\rho_0$  is the Boussinesq reference density, and  $r_b$  is the linear bottom friction  
 260 coefficient. Since  $\langle \bar{\tau}_x \rangle$ ,  $\rho_0$  and  $r_b$  are the same for both control experiments,  
 261 the zonally-averaged zonal flow in their model bottom level,  $\langle \bar{u}_b \rangle$ , must also  
 262 be roughly the same. In a model with bathymetry high enough so as to  
 263 block geostrophic contours, the near bottom flow is much weaker and  $T_b$   
 264 correspondingly lower (see, e.g., Munday et al., 2015).

265 The thermal wind transport of both controls is below that of the real  
 266 ACC, which recent estimates place at around 134Sv (Meredith et al., 2011).  
 267 This is due to a combination of factors that include the cross-channel tem-  
 268 perature difference being lower than in some parts of the SO and the stratifi-  
 269 cation also being potentially shallower than in some locations. These would  
 270 combine to give a lower thermal wind shear than in the real SO and therefore  
 271 a lower  $T_{tw}$ .

### 272 3.2. Residual Overturning of the Control State

273 [Figure 5 about here.]

274 Following AMF11 and ZM14/MZ15, the model’s residual overturning,  
 275  $\Psi_{\text{res}}$ , is calculated using temperature as the vertical coordinate and re-binning

the model's meridional velocities into temperature layers  $0.2^{\circ}\text{C}$  thick. This is an online calculation that includes information from every model timestep to ensure that high frequency motions are captured. The RMOC is then mapped back to vertical coordinates using the time and zonal mean thickness of each temperature layer. The bolus overturning,  $\Psi^*$ , due to the integral effects of the vigorous mesoscale eddy field, can then be calculated as the difference between  $\Psi_{\text{res}}$  and the Eulerian overturning,  $\bar{\Psi}$ , calculated from the time-average meridional velocity field.

Broadly speaking the RMOCs for the two control experiments look very similar to, and have much in common with, the control experiment RMOCs of AMF11 and ZM14/MZ15. As shown in Fig. 5, they consist of model analogues of the clockwise North Atlantic Deep Water (NADW) cell and the anticlockwise Antarctic Bottom Water (AABW) cell. An Antarctic Intermediate Water (AAIW) cell also forms near the northern boundary, close to the northern boundary restoring zone. The most noticeable difference between the two RMOC's in Fig. 5 is that the stochastic wind stress experiment has slightly stronger upwelling in its NADW cell and a slightly weaker AABW cell.

In terms of the Southern Ocean's actual RMOC, both the stochastic and equivalent stress control experiments are of the right order of magnitude, with peak values of the NADW cell at  $0.72\text{Sv}$  and  $0.61\text{Sv}$ , respectively. Scaling the model domain up to the full extent of the real SO, a factor of 20-25, would give peak values of  $14.4 - 18\text{Sv}$  and  $12.2 - 15.25\text{Sv}$ . Estimates place the upwelling of the Southern Ocean in the  $10 - 20\text{Sv}$  range (Marshall et al., 2006; Lumpkin and Speer, 2007).



Fig. 5 also shows that the mixed layer, defined as above the depth at which the water is  $0.8^{\circ}\text{C}$  colder than the surface (above the grey line in Fig. 5, see, e.g., Kara et al. (2000), for details), is slightly deeper for the stochastic wind stress control. This is consistent with the increased vertical viscosity/diffusivity provided by KPP as a result of the stochastic variation of the wind stress leading to surface-intensified mixing. These are reported in Table 2 as domain average values of  $45/42\text{cm}^2\text{s}^{-1}$  for the stochastic control, compared with  $24/18\text{cm}^2\text{s}^{-1}$  for the equivalent wind stress control. This elevated mixing drives deepening of the mixed layer, as noted above, and may make contributions to, for example, the budgets of momentum, kinetic energy, temperature and temperature variance.

#### 4. Sensitivity of the Energy Budget to Wind Stress Variability

##### 4.1. Simple Energy Budget Diagnostics

[Figure 6 about here.]

As  $\sigma_{\tau}$  increases in the stochastic wind stress experiments, the peak wind stress increases as per Fig. 4, as it also does for the equivalent wind stress experiments by construction. The stronger wind stress also does more work at the surface, and thus power input into the model's circulation is higher. Despite the mean wind stress being the same, the stochastic wind stress experiments have considerably more power entering the circulation via surface wind work than the equivalent wind stress experiments (Fig. 6a, cf. blue and red dots). This is due to the strong correlation in time between the stochastic perturbations to the wind stress and the resulting ocean currents.

324 The surface wind work can be Reynolds averaged to write  $\overline{\boldsymbol{\tau} \cdot \mathbf{u}_s} = \overline{\boldsymbol{\tau}} \cdot$   
 325  $\overline{\mathbf{u}_s} + \overline{\boldsymbol{\tau}' \cdot \mathbf{u}_s'}$ , with the subscript  $s$  indicating surface values. Diagnosis of  
 326 this decomposition for the stochastic wind stress experiments shows that an  
 327 increasingly large fraction of the power input from the wind stress comes  
 328 from the wind stress perturbations acting upon the velocity perturbations  
 329 (Fig. 6a, cf. blue and green dots). However, the work done by the mean  
 330 wind on the mean flow, i.e. the first term on the right-hand side of the above  
 331 decomposition, remains comparable to the total wind work in the equivalent  
 332 wind stress experiments (Fig. 6a, cf. red and green dots).

333 Surface wind work is estimated to input approximately 1TW of power into  
 334 the ocean circulation, with about half of this occurring in the SO (Wunsch  
 335 and Ferrari, 2004; Ferrari and Wunsch, 2009). The power input in the two  
 336 control simulations is 0.071TW and 0.044TW for the stochastic wind stress  
 337 and equivalent wind stress control experiments, respectively. Scaling this  
 338 up to the full extent of the SO, using a factor of 20-25, gives figures of  
 339 1.42 – 1.78TW and 0.88 – 1.1TW. Both these figures are over-estimates  
 340 caused by the strong zonal surface flow that results from using a flat bottom  
 341 and thus very strong correlation between the surface currents and the wind  
 342 stress. However, it is the surface wind stress operating on the baroclinic  
 343 shear that provides the power to drive the eddy energy (Abernathey et al.,  
 344 2011) and so this excess power input should not invalidate our results.

345 Following Cessi et al. (2006) and Cessi (2008), the leading order mechan-  
 346 ical eddy budget of the model is expected to be

$$\langle \overline{\boldsymbol{\tau} \cdot \mathbf{u}_s} \rangle \approx \rho_0 r_b \langle \overline{\mathbf{u}_b \cdot \mathbf{u}_b} \rangle. \quad (8)$$

348 Applying Reynolds averaging to Eq. (8) gives

$$349 \quad \langle \bar{\boldsymbol{\tau}} \cdot \bar{\mathbf{u}}_s \rangle + \langle \overline{\boldsymbol{\tau}' \cdot \mathbf{u}'_s} \rangle \approx \rho_0 r_b \langle \bar{\mathbf{u}}_b \cdot \bar{\mathbf{u}}_b \rangle + \rho_0 r_b \langle \overline{\mathbf{u}'_b \cdot \mathbf{u}'_b} \rangle. \quad (9)$$

350 This approximate budget states that the power input by the surface wind  
351 work is balanced by bottom friction dissipation acting on the total kinetic  
352 energy. Due to the flat bottomed nature of the channel, we must retain the  
353 mean kinetic energy dissipation on the right-hand-side of Eq. (9).

354 The left- and right-hand sides of Eq. (9) are diagnosed in Fig. 6b. The  
355 blue dots show the total power input due to wind stress against the total  
356 bottom dissipation, i.e. the left-hand side of Eq. (8) plotted against its  
357 right-hand side, for the stochastic wind stress experiments. The red dots are  
358 the same diagnostics for the equivalent wind stress experiments. However,  
359 the green dots plot the total bottom dissipation against the power input  
360 from the mean wind acting on the mean flow, i.e. the right-hand side of  
361 Eq. (9) against only the first term on its left-hand side. This highlights that  
362 the strong correlation between the time-varying wind and the time-varying  
363 ocean currents **provides more power than the resulting flow can dissipate** by  
364 bottom friction processes alone. In contrast, the bottom dissipation of total  
365 kinetic energy is sufficient to roughly balance the total wind work for the  
366 equivalent wind stress experiments (Fig. 6b, red dots).

367 [Figure 7 about here.]

368 In a viscid fluid, viscosity redistributes momentum and dissipates energy,  
369 and so changes in viscosity can affect the dissipation of total kinetic energy.  
370 Examining the average diffusivities and viscosities that KPP calculates shows

a large increase over the range of wind forcing considered. In particular, the vertical diffusivity/viscosity for any given stochastic wind stress experiment is always higher than its in partner equivalent wind stress experiment, see Fig. 7. The “missing” energy dissipation may therefore be accounted for by vertical viscous dissipation. It is also possible that horizontal viscous forces may remain equally, or more, important than vertical ones. Therefore, in Section 4.2 we turn to a more complete estimate of the sinks and sources of power within the model via the mechanical energy framework of Winters et al. (1995).

#### 4.2. Full Power Budget Diagnostics

Deriving a full mechanical energy budget for the ocean, particularly in the presence of a nonlinear equation of state, is complicated by the large gravitational potential energy of its stratification. This has led to a number of different formulations based upon the earlier work of Winters et al. (1995). The key difference between these formulations lies in their treatment of the background gravitational potential energy, e.g. Tailleux (2009, 2013) vs. Hughes et al. (2009) and Saenz et al. (2012), and the amount available for potential energy to kinetic energy conversions. Recently, dynamical potential energy was proposed as a way to eliminate some of the complications inherent to calculations of **Available Potential Energy (APE)** by defining a new pressure variable (Roquet, 2013).

A complete treatment of the (available) potential energy, and thus the full mechanical energy budget, is beyond the scope of this paper. Instead, we concentrate on the changes to the kinetic energy budget due to a stochastic wind stress and outline the framework of Winters et al. (1995), using the

notation due to Hughes et al. (2009) and Hogg et al. (2013).

The volume integrated kinetic energy budget for a Boussinesq fluid is given by (Winters et al., 1995; Hughes et al., 2009; Hogg et al., 2013)

$$\rho_0 \frac{\partial E_k}{\partial t} = \Phi_\tau - \Phi_z - \Phi_r - \epsilon, \quad (10)$$

where  $E_k$  is the volume integrated kinetic energy given by

$$E_k = \frac{1}{2} \int_V \overline{u^2 + v^2} dV, \quad (11)$$

and  $V$  is the volume of the model ocean. Henceforth, we assume statistical steady state such that the left-hand-side of Eq. (10) is zero.  $\Phi_\tau$  is the power source due to surface wind stress,  $\Phi_z$  is the conversion between kinetic and potential energy,  $\Phi_r$  is the power sink due to bottom friction, and  $\epsilon$  is the power sink due to viscous stresses.

Surface wind stress does work on the surface currents and so acts as a source of power. For a time-varying wind stress, such as in our stochastic wind stress experiments, there are two components to the surface wind work, as per Eq. (9). The first is due to the mean wind stress acting on the mean surface velocities,  $\Phi_{\bar{\tau}}$ , and the second is due to wind stress perturbations acting on the surface perturbation velocities,  $\Phi_{\tau'}$ , i.e.  $\Phi_\tau = \Phi_{\bar{\tau}} + \Phi_{\tau'}$ . These two components are given by

$$\Phi_{\bar{\tau}} = \int_S \bar{\boldsymbol{\tau}} \cdot \bar{\mathbf{u}}_s dS, \quad (12)$$

$$\Phi_{\tau'} = \int_S \overline{\boldsymbol{\tau}' \cdot \mathbf{u}'_s} dS, \quad (13)$$

where  $S$  is the surface of the ocean.

The conversion between kinetic and potential energy, found to be small with respect to the main sources and sinks in the experiments presented here and thus henceforth neglected, is given by

$$\Phi_z = \int_V \overline{\rho g w} \, dV. \quad (14)$$

Linear bottom friction acts as a sink of power at the bottom of the model domain. In an ocean with significant bathymetry, this sink is expected to be dominated by the contribution from EKE (Cessi et al., 2006; Cessi, 2008). However, we must retain the term due to dissipation of mean kinetic energy at the bottom, as per Eq. (9). Hence, we write this sink as

$$\Phi_r = \int_S \rho_0 r_b \overline{\mathbf{u}_b \cdot \mathbf{u}_b} \, dS. \quad (15)$$

The dissipation of kinetic energy due to viscous stresses is divided into two parts, that due to horizontal viscosity,  $\epsilon_h$ , and that due to vertical viscosity,  $\epsilon_v$ , i.e.  $\epsilon = \epsilon_h + \epsilon_v$ . These two components are given by

$$\epsilon_h = \rho_0 \int_V A_4 \overline{\nabla_h u \cdot \nabla_h (\nabla_h^2 u)} + A_4 \overline{\nabla_h v \cdot \nabla_h (\nabla_h^2 v)} \, dV, \quad (16)$$

$$\epsilon_v = \rho_0 \int_V A_v \overline{\frac{\partial \mathbf{u}_h}{\partial z} \cdot \frac{\partial \mathbf{u}_h}{\partial z}} \, dV, \quad (17)$$

where the subscript  $h$  implies the horizontal component of the vector under consideration. Note that the vertical viscosity,  $A_v$ , may vary in time due to the use of the KPP parameterisation and is harmonic. In contrast, the horizontal biharmonic viscosity,  $A_4$ , is a constant in space and time.

### 4.3. Sensitivity to Wind Stress of the Full Power Budget

Estimates of  $\Phi_{\bar{\tau}}$ ,  $\Phi_{\tau'}$ ,  $\Phi_r$ ,  $\epsilon_h$  and  $\epsilon_v$  were obtained from the 50-year diagnostic run at statistical steady state. The changes that the sources and sinks undergo is best illustrated by considering the control wind stress and extreme wind stress cases for the stochastic and equivalent wind stress experiments. It is also useful to consider both the absolute and relative magnitude for each term, as done in Figure 8. This highlights that there are changes in the partitioning of dissipation between bottom friction and vertical viscous dissipation as the variability of the atmospheric wind changes.

[Figure 8 about here.]

As the variability of the wind increases, so does the surface wind stress, as shown in Fig. 4, and thus the power source to the ocean circulation also increases (Fig. 6a). In terms of the framework outlined in Section 4.2,  $\Phi_{\bar{\tau}}$  and  $\Phi_{\tau'}$  both increase. However, the fraction of the total power input that comes from the mean wind stress acting on the mean ocean velocities decreases. For the extreme stochastic wind stress experiment, roughly 2/3 of the total power provided to the ocean circulation by the wind is due to  $\Phi_{\tau'}$ . In contrast, at the control wind stress around 1/3 of the power input to the ocean comes from  $\Phi_{\tau'}$  (Fig. 8b, 1st and 3rd columns).

For all of the equivalent wind stress experiments,  $\Phi_{\tau'} = 0$  by construction, and so the source of power at the surface is reduced. However, the magnitude of  $\Phi_{\bar{\tau}}$  remains roughly the same between matched pairs of equivalent and stochastic wind stress experiments (see Figs. 6a and 8a, 3rd and 7th columns).

462 For the extreme wind stress experiments, there is a disparity between  
 463 the time-mean vertical viscosity that is provided by KPP between pairs of  
 464 stochastic and equivalent wind stress experiments (see Fig. 7a). The equiv-  
 465 alent wind stress extreme shows an increase in magnitude for the dissipation  
 466 of KE due to vertical viscosity, relative to the control experiment (cf. Fig.  
 467 8a, 6th and 8th columns). However, the fraction of dissipation is roughly  
 468 the same as the control (cf. Fig. 8b, 6th and 8th column). This is a strong  
 469 contrast with the stochastic wind stress extreme experiment, which has more  
 470 power dissipated by vertical viscosity than it does by linear bottom friction  
 471 (Fig. 8a, 4th column). Furthermore, the fraction of power dissipated by ver-  
 472 tical viscosity also increases between the stochastic wind stress control and  
 473 extreme (Fig. 8b, 2nd and 4th column). This fractional increase is roughly  
 474 in proportion to the fractional increase in power supplied by  $\Phi_{\tau'}$  with respect  
 475 to  $\Phi_{\bar{\tau}}$ .

476 In summary, increasing the wind power input to the ocean causes an in-  
 477 crease in the power dissipated by bottom friction. However, in the case of the  
 478 stochastic wind stress experiments, the increase in the power dissipated by  
 479 vertical viscous processes, i.e. KPP, increases by a greater proportion. This  
 480 leads to a change in the dominant power dissipation mechanism, consistent  
 481 with the results of Jouanno et al. (2016). For both sets of experiments, the  
 482 change in energy dissipation due to horizontal viscosity remains relatively  
 483 small. This increase in vertical viscous dissipation is brought about by the  
 484 increase in the vertical viscosity provided by KPP (see Fig. 7).



## 5. Sensitivity to Wind Stress of the Circulation

### 5.1. Sensitivity to Wind Stress of the Temperature Field and Zonal Transport

[Figure 9 about here.]

The increase in KPP's vertical viscosity shown in Fig. 7b alters the power budget of the model, such that at extreme wind stress variability more power is dissipated by vertical viscous processes than bottom friction. The increase in KPP's vertical diffusivity may also influence the model by dissipating temperature variance/potential energy. However, rather than diagnose the potential energy budget, it is simpler to examine the temperature structure as an overall summary of stratification and thermal wind shear changes.

The impact of the buoyancy budget alteration by high near-surface vertical diffusivity can be seen in Fig. 9, which shows the time and zonal average of potential temperature for the control and extreme experiments. The control experiments in Fig. 9a have similar stratification, allowing for the slightly deeper mixed layer in the stochastic control. For the extreme stochastic experiment in Fig. 9b, the increase in the mixed layer diffusivity has led to nearly vertical isotherms near the surface, but flatter isotherms at depth than the extreme equivalent experiment. This reduces the cross-channel buoyancy difference over most of the depth for the extreme stochastic wind stress experiment. Hence, its  $T_{tw}$  is lower than the extreme equivalent wind stress experiment. In fact, as shown in Fig. 10 the control stochastic wind stress experiment actually has the highest  $T_{tw}$  of all the stochastic experiments.

[Figure 10 about here.]

At low wind stresses,  $\tau_0 < 0.2\text{Nm}^{-2}$ , both sets of experiments have very similar  $T_{tw}$ . At these low stresses, not all isotherms outcrop at the surface, and so the cross-channel buoyancy difference is lower than in the two controls, leading to a reduced  $T_{tw}$ . As the wind stress increases, the two sets of experiments differ from each other. For the equivalent wind stress experiments,  $T_{tw}$  increases quasi-linearly, much as with the experiments of MZ15. However, the thermal wind transport of the stochastic wind stress experiments begins to decrease and all 4 experiments with a peak mean wind stress greater than the control actually have a lower  $T_{tw}$  than the control. This is most likely due to the exceptionally large changes in the diffusivity that KPP prescribes as  $\sigma_\tau$  increases. Whilst this steepens the isopycnals in the mixed layer, it leads to less steep isopycnals outside of the mixed layer, essentially via geometry, and a reduced cross-channel buoyancy difference.

At a finer grid spacing, and/or higher wind stress, both the stochastic and equivalent wind stress may demonstrate a higher degree of eddy saturation than that in Fig. 10. However, it is impossible to say without running the experiments at considerable computational expense. It seems likely, however, that, should further increases in wind stress saturate the transport, then the stochastic wind stress experiments would achieve a substantially lower final transport than the equivalent wind stress experiments.

Changing wind stress can also alter  $T_{ACC}$  by  $T_b$ . However, by construction, the equivalent wind stress experiments use wind stress diagnosed from their stochastic partner. Hence, matched pairs of experiments have very similar  $T_b$  (not shown).

## 5.2. Sensitivity to Wind Stress of the RMOC

[Figure 11 about here.]

To examine the sensitivity of the RMOC to changes in wind stress, the RMOC is first quantified in a simple manner. To do so, we use the same method as AMF11 and select the maximum and minimum value of  $\Psi_{\text{res}}$  below 500 m and 100 km south of the edge of the sponge region. These values are labeled  $\Psi_{\text{upper}}$  and  $\Psi_{\text{lower}}$  for the NADW and AABW cells, respectively. As qualitatively described in Section 3.2,  $\Psi_{\text{upper}}$  and  $\Psi_{\text{lower}}$  indicate a stronger NADW but weaker AABW cell under stochastic wind stress for the control experiments (see Table 2).

Fig. 11a shows the variation of  $\Psi_{\text{upper}}$  and  $\Psi_{\text{lower}}$  (blue/red symbols respectively) across both sets of experiments, as well as the maximum Eulerian overturning ( $\bar{\Psi}_{\text{max}}$ , black dots) for the stochastic wind stress experiments as a comparison. The difference between  $\Psi_{\text{upper}}$  for the stochastic and equivalent wind stress experiments becomes accentuated at peak mean wind stresses  $> 0.2\text{Nm}^{-2}$ . In contrast,  $\Psi_{\text{lower}}$  shows that there is little real difference in the sensitivity AABW cell across the wide range of wind stresses considered. The value of  $\Psi_{\text{lower}}$  for the stochastic wind stress experiment where  $\sigma_{\tau} = 21\text{ms}^{-1}$  is something of an outlier. The extreme variability of the wind has caused the mixed layer to deepen to such an extent that it impinges upon the upper limit, 500m, of the streamfunction values tested for this diagnostic. As a result,  $\Psi_{\text{lower}}$  starts to represent the mixed layer overturning rather than the strength of the AABW cell.

Using residual mean theory the RMOC's streamfunction can be written as the sum of the Eulerian mean MOC ( $\bar{\Psi}$ ) and the eddy-induced bolus

557 overturning ( $\Psi^*$ ) (see, e.g., Marshall and Radko, 2003), i.e.

$$558 \quad \Psi_{\text{res}} = \bar{\Psi} + \Psi^* = -\frac{\langle \bar{\tau}_x \rangle}{\rho_0 f} + K s, \quad (18)$$

559 where  $f$  is the Coriolis parameter,  $K$  is the quasi-Stokes/eddy diffusivity for  
 560 the buoyancy field ( $b = -g(\rho - \rho_0)/\rho_0$ ) and  $s = -\bar{b}_y/\bar{b}_z$  is the isopycnal slope.  
 561 Following MZ15, we take small perturbations around Eq. (18) and write

$$562 \quad \Delta \Psi_{\text{res}} \approx -\frac{\Delta \bar{\tau}_x}{\rho_0 f} + \Delta K s_0 + K_0 \Delta s, \quad (19)$$

563 where  $K_0$  and  $s_0$  are the eddy diffusivity and isopycnal slope of a chosen  
 564 equivalent wind stress experiment. Dividing by  $\Psi_0^* = K_0 s_0$ , the unperturbed  
 565 bolus overturning, and writing  $\Delta \bar{\Psi} = -\Delta \bar{\tau}_x / \rho_0 f$ , the change in the residual  
 566 overturning as a fraction of the original bolus overturning is related to changes  
 567 in mean wind stress,

$$568 \quad \frac{\Delta \Psi_{\text{res}}}{\Psi_0^*} \approx \frac{\Delta \bar{\Psi}}{\Psi_0^*} + \frac{\Delta K}{K_0} + \frac{\Delta s}{s_0}. \quad (20)$$

569 By construction,  $\Delta \bar{\Psi} \approx 0$  between pairs of stochastic wind stress and  
 570 equivalent wind stress experiments. Therefore, fractional changes in the  
 571 residual overturning between pairs must be related to a combination of  
 572 changes in isopycnal slope and eddy diffusivity. If there were no changes  
 573 in  $\Delta \Psi_{\text{res}}/\Psi_0^*$ , then the fractional change in isopycnal slope can be simply  
 574 related to the fractional change in eddy diffusivity, i.e.

$$575 \quad \frac{\Delta s}{s_0} \approx -\frac{\Delta K}{K_0}. \quad (21)$$

We have already seen that increasing  $\sigma_\tau$  leads to reduced (more positive) isopycnal slopes, which gives  $\Delta s/s_0 < 0$ . This implies that to maintain the RMOC at the equivalent wind stress experiment values, the eddy diffusivity of the stochastic wind stress experiments would have to increase. This would be consistent with the elevated levels of EKE seen in the stochastic wind stress experiments. However, these elevated levels are biased to the near surface values and it is the isopycnal slope and eddy diffusivity outside of the mixed layer that set  $\Psi_{\text{res}}$

To quantitatively examine the relationship encoded in Eqs. (20) and (21), we diagnose the mean eddy diffusivity in each of our experiments using a simple flux gradient closure, i.e.

$$\langle \overline{v'\theta'} \rangle = -K \left\langle \frac{\partial \bar{\theta}}{\partial y} \right\rangle. \quad (22)$$

The eddy diffusivity and isopycnal slope are then averaged over the central 500km of the channel between depths of 1100m and 1800m. Perturbations are taken between pairs of stochastic wind stress and equivalent wind stress experiments, with the equivalent wind stress experiment taken as the initial solution for the purposes of Eq. (20).

[Figure 12 about here.]

Plotting  $-\Delta K/K_0$  against  $\Delta s/s_0$  in Fig. 12a shows that the fractional change in eddy diffusivity is of the opposite sense to that required for maintenance of the RMOC in the stochastic wind stress experiments. In other words, both the isopycnal slope and eddy diffusivity has decreased between pairs of equivalent and stochastic wind stress experiments. This means that

the bolus overturning must decrease and the RMOc must also change, as previously highlighted in Fig. 11. In effect, the decrease in the bolus overturning allows more of the Eulerian mean flow to show and the result is a stronger RMOc under stochastic wind stress.

As a final check on Eq. (20), we have also included  $\Delta\Psi_{\text{res}}/\Psi_0^*$  and  $\Delta\bar{\Psi}/\Psi_0^*$  on the y-axis of Fig. 12b. In this case, the relationship holds well, indicating that the neglected terms that are quadratic in perturbation terms in Eq. (20) are small and that our diagnosis of the eddy diffusivity and isopycnal slope are accurate enough to properly capture the physics of the changes.

## 6. Discussion and Conclusions

The Southern Ocean is important to climate because of its residual circulation and the Antarctic Circumpolar Current, which allow for meridional and zonal exchange of properties between ocean basins (Meredith et al., 2011). Understanding the processes and mechanisms that set its circulation, and its sensitivity to changing forcing, are therefore of paramount importance to understanding global climate.

Numerous numerical models indicate that the sensitivity to wind stress of the RMOc and volume transport of the ACC are reduced in the presence of a resolved or permitted eddy field (see, e.g., Hallberg and Gnanadesikan, 2006; Munday et al., 2013). Many investigations into these phenomena rely upon the use of idealised wind stress patterns that are constant in time. However, the mean wind stress felt by the ocean is a function of both the mean atmospheric wind and its variability. Changing a constant mean wind stress implicitly assumes that the stress is becoming greater due to a stronger

mean wind.

Here we have investigated the impact that changing the variability of the atmospheric wind, whilst keeping the mean atmospheric wind constant, has upon the Southern Ocean circulation. We performed two sets of experiments with the same mean wind stress. The stochastic wind stress experiments had their atmospheric wind altered by a pseudo-random number from a white Gaussian distribution every 6 hours. This random number was multiplied by a chosen standard deviation to give a range of wind stress. The equivalent wind stress experiments are driven by the time-mean wind from their corresponding stochastic wind stress partner.

At the control wind stress of  $\sim 0.17\text{Nm}^{-2}$  there are only minor differences between the stochastic and equivalent wind stress circulations. The RMO is composed of NADW and AABW cells of similar strength (see Table 2) and the circumpolar transport due to thermal wind shear is also similar. This implies that there is also only minor changes in the north-south buoyancy difference across the channel and thus the isopycnal slope. The mixed layer is deeper with stochastic wind stress, which gives stronger viscosity/diffusivity in the mixed layer from the KPP parameterisation.

As the mean wind stress is altered, the stochastic and equivalent wind stress experiments deviate from each other in terms of their RMO and circumpolar transport. The deep RMO of the equivalent wind stress experiments is less sensitive to the changing wind stress than in their stochastic partners. In addition, the equivalent wind stress experiments show indications of the emergence of eddy saturation. This contrasts with the stochastic wind stress experiments, for which an increase in the variability of the at-

648 mospheric wind, and thus the mean wind stress, results in a reduction of the  
649 circumpolar transport.

650     Diagnosis of the power budget for kinetic energy indicates that the rise in  
651 viscosity/diffusivity from KPP goes hand-in-hand with an increase in power  
652 dissipation due to vertical viscosity. This results in a change in the dominant  
653 power dissipation **mechanism**, from bottom drag to near-surface viscous pro-  
654 cesses, for the stochastic wind stress experiments as the variability of the wind  
655 is increased. **This may well be accompanied by changes in energy pathways**  
656 **between, e.g., forcing and EKE. For example, in a simple channel model with**  
657 **a periodically varying wind stress, Sinha and Abernathey (2016) see peaks in**  
658 **the EKE spectra corresponding to wind variation with periodicity of longer**  
659 **than a year. However, the APE spectra continues to display peaks for higher**  
660 **frequency wind forcing. At these high frequencies, they find the conversion**  
661 **from APE to EKE is small and relate this to changes in the pathways be-**  
662 **tween energy reservoirs. Proper verification of such a change in our model**  
663 **would require diagnosis of the (available) potential energy and its budget.**

664     The increased near-surface vertical temperature diffusivity deepens the  
665 mixed layer and ultimately results in flatter isotherms over most of the chan-  
666 nel. **These flatter isotherms eventually lead to a decrease in circumpolar**  
667 **transport with increasing wind variability, which contrasts with the increas-**  
668 **ing circumpolar transport seen in the equivalent wind stress experiments. In**  
669 **addition, the flatter isotherms ultimately reduce the eddy diffusivity such**  
670 **that the bolus overturning starts to weaken at high wind stress variability.**  
671 **This leads to a stronger sensitivity to wind stress of the RMOC in the stochas-**  
672 **tic wind stress experiments as more of the Eulerian overturning is “seen” in**



673 the residual flow.

674 Our main conclusion is that changes in the variability of the atmospheric  
 675 wind may lead to considerably different sensitivity of the RMOC and volume  
 676 transport of the ACC than that caused by blowing a stronger mean wind  
 677 over the ocean. In this model, KPP interprets the increased near surface  
 678 shear due to the variable wind as increased viscous and diffusive mixing.  
 679 This deepens the mixed layer and contributes a strong diabatic aspect to  
 680 the near-surface RMOC. It is something of a concern that this conclusion is  
 681 so strongly tied to a parameterised, rather than resolved, physical process.  
 682 This is because it is possible that KPP may not be representing the instability  
 683 and mixing processes in a completely physical way, i.e. KPP translates the  
 684 increased near-surface shear into near-surface mixing without allowing for,  
 685 e.g., the vertical propagation of waves that might lead to increased mixing  
 686 at depth. Such vertical propagation would surely produce different degrees  
 687 of eddy saturation and eddy compensation than in our simple flat-bottomed  
 688 channel model. However, even if the response of KPP is not precisely correct  
 689 in physical terms, our results indicate that assessing whether wind stress  
 690 changes due to increasing mean wind or increasing variability is of potential  
 691 concern for the response of the ocean circulation and climate as a whole.

692 The real ocean is predominantly inviscid. However, our conclusion, that  
 693 the dominant kinetic energy sink may change from bottom friction processes  
 694 to near-surface mixing processes and lead to altered sensitivity of the ocean's  
 695 stratification and RMOC to wind stress, can still hold in these conditions.  
 696 This is because KPP is parameterising a number of mixing processes. Whilst  
 697 these processes may not be viscous and/or diffusive in the real ocean, this

698 is how KPP represents them. Hence, the transition to a new dominant  
 699 dissipative process is still valid, even if in the real ocean that process is not  
 700 viscous or diffusive. In this case, whilst the details of how the stratification  
 701 and RMO change may differ, that a change in the energy budget could  
 702 influence their sensitivity to wind stress changes could remain.

703 The geometry and complexity of the real ocean's bottom bathymetry is  
 704 not well represented by our model's flat bottom. This could potentially be  
 705 troublesome in the SO, where bottom form stresses across large bathymetric  
 706 obstacles balances the momentum input from the wind (Munk and Palmén,  
 707 1951; Johnson and Bryden, 1989). This is our reason for primarily focussing  
 708 on the energy budget of the ocean in our analysis; pressure gradients, and by  
 709 extension bottom form stresses, do not enter into the energetics framework of  
 710 Winters et al. (1995) or play a role in the energy cycle (Ferrari and Wunsch,  
 711 2009). As a result, even with large bottom bathymetry, the zero order power  
 712 budget can be expected to be that of Cessi et al. (2006) and Cessi (2008), i.e.  
 713 surface wind work balanced by bottom EKE dissipation. The key change here  
 714 from our model's budget is that we must retain the dissipation from mean  
 715 bottom currents in Eqs. (8) and (9). The strong bottom flow in our flat  
 716 bottomed model also leads to a disproportionately large power input. These  
 717 could combine to potentially influence the level of wind variability required  
 718 to bring about a transition in the dominant energy dissipation mechanism  
 719 in a model with complex bathymetry and more realistic power input. The  
 720 assessment of the power budget in such a model, and how the budget changes  
 721 under more variable wind forcing, is therefore the next step.

## Acknowledgements

DRM is supported by the Natural Environment Research Council [ORCHESTRA, grant number NE/N018095/1]. Much of this work took place whilst DRM was a PDRA at the Department of Physics in the University of Oxford and was supported by the UK Natural Environment Research Council. DRM thanks Scott Bachman and Alberto Naveira Garabato for helpful discussions. The authors thank two anonymous reviewers whose comments improved the presentation of the paper. This work made use of the facilities of HECToR, the UK's national high-performance computing service, which is provided by UoE HPCx Ltd at the University of Edinburgh, Cray Inc and NAG Ltd, and funded by the Office of Science and Technology through EPSRC's High End Computing Programme. This work used the ARCHER UK National Supercomputing Service (<http://www.archer.ac.uk>). Model output is available from DRM upon request.

## References

- Abernathy, R., Marshall, J., Ferreira, D., 2011. The dependence of Southern Ocean meridional overturning on wind stress. *J. Phys. Oceanogr.* 41, 2261–2278.
- Bryan, K., Cox, M. D., 1972. An approximate equation of state for numerical models of ocean circulation. *J. Phys. Oceanogr.* 2, 510–517.
- Bryden, H. L., 1979. Poleward heat flux and conversion of available potential energy in Drake Passage. *J. Mar. Res.* 37, 1–22.

- 744 Cessi, P., 2008. An energy-constrained parameterization of eddy buoyancy  
745 flux. *J. Phys. Oceanogr.* 38, 1807–1820.
- 746 Cessi, P., Young, W. R., Polton, J. A., 2006. Control of large-scale heat  
747 transport by small-scale mixing. *J. Phys. Oceanogr.* 36, 1877–1894.
- 748 Delworth, T. L., Rosati, A., Anderson, W., Adcroft, A. J., Balaji, V., Benson,  
749 R., Dixon, K., Griffies, S. M., Lee, H.-C., Pacanowski, R. C., Vecchi,  
750 G. A., Wittenberg, A. T., Zeng, F., Zhang, R., 2012. Simulated climate  
751 and climate change in the GFDL CM2.5 high-resolution coupled climate  
752 model. *J. Clim.* 25, 2755–2781.
- 753 Ferrari, R., Wunsch, C., 2009. Ocean circulation kinetic energy: Reser-  
754 voirs, sources, and sinks. *Annu. Rev. Fluid Mech.* 41, 253–282,  
755 doi:10.1146/annurev.fluid.40.111406.102139.
- 756 Furuichi, N., Hibiya, T., Niwa, Y., 2008. Model-predicted distribution of  
757 wind-induced internal wave energy in the world’s ocean. *J. Geophys. Res.*  
758 113, C09034, doi:10.1029/2008JC004768.
- 759 Gill, A. E., Bryan, K., 1971. Effects of geometry on the circulation of a  
760 three-dimensional southern-hemisphere ocean model. *Deep-Sea Res.* 18,  
761 685–721.
- 762 Hallberg, R., Gnanadesikan, A., 2006. The role of eddies in determining the  
763 structure and response of the wind-driven southern hemisphere overturn-  
764 ing: Results from the Modeling Eddies in the Southern Ocean (MESO)  
765 project. *J. Phys. Oceanogr.* 36, 2232–2252.

- 766 Hogg, A. M., Dijkstra, H. A., Saenz, J. A., 2013. The energetics of a collapsing  
767 meridional overturning circulation. *J. Phys. Oceanogr.* 43, 1512–1524.
- 768 Hogg, A. M., Munday, D. R., 2014. Does the sensitivity of Southern Ocean  
769 circulation depend upon bathymetric details? *Phil. Trans. R. Soc A* 372,  
770 20130050, doi:10.1098/rsta.2013.0050.
- 771 Hughes, G. O., Hogg, A. M., Griffiths, R. W., 2009. Available potential  
772 energy and irreversible mixing in the meridional overturning circulation.  
773 *J. Phys. Oceanogr.* 39, 3130–3146.
- 774 Jayne, S. R., Marotzke, J., 2002. The oceanic eddy heat transport. *J. Phys.*  
775 *Oceanogr.* 32, 3328–3345.
- 776 Johnson, G. C., Bryden, H. L., 1989. On the size of the Antarctic Circumpolar  
777 Current. *Deep-Sea Res.* 36, 39–53.
- 778 Jouanno, J., Capet, X., Madec, G., Roulet, G., Klein, P., 2016. Dissipation of  
779 the energy imparted by mid-latitude storms in the southern ocean. *Ocean*  
780 *Sci.* 12, 743–769, doi:10/5194/os-12-743-2016.
- 781 Kalnay, E., Kanamitsu, M., Kistler, R., Collins, W., Deaven, D., Gandin,  
782 L., Iredell, M., Saha, S., White, G., Woollen, J., Zhu, Y., Chelliah, M.,  
783 Ebisuzaki, W., Higgins, W., Janowiak, J., Mo, K. C., Ropelewski, C.,  
784 Wang, J., Leetmaa, A., Reynolds, R., Jenne, R., Joseph, D., 1996. The  
785 NCEP/NCAR 40-year reanalysis project. *Bull. Amer. Met. Soc.* 77, 437–  
786 471.

- 787 Kara, A. B., Rochford, P. A., Hurlburt, H. E., 2000. An optimal defini-  
 788 tion for ocean mixed layer depth. *J. Geophys. Res.* 105, 16 803–16821,  
 789 doi:10.1029/2000JC900072.
- 790 Large, W. G., McWilliams, J. C., Doney, S. C., 1994. Oceanic vertical mixing:  
 791 A review and a model with a nonlocal boundary layer parameterization.  
 792 *Rev. Geophys.* 32, 363–403.
- 793 Large, W. G., Pond, S., 1981. Open ocean momentum flux measurements in  
 794 moderate to strong winds. *J. Phys. Oceanogr.* 11, 324–336.
- 795 Lumpkin, R., Speer, K., 2007. Global ocean meridional overturning. *J. Phys.*  
 796 *Oceanogr.* 37, 2550–2562, doi:10.1175/JPO3130.1.
- 797 Marsaglia, G., Bray, T. A., 1964. A convenient method for generating normal  
 798 variables. *SIAM Rev.* 6, 260–264, doi:10.1137/1006063.
- 799 Marshall, J., Adcroft, A., Hill, C., Perelman, L., Heisey, C., 1997a. A finite  
 800 volume, incompressible Navier-Stokes model for studies of the ocean on  
 801 parallel computers. *J. Geophys. Res.* 102, 5753–5766.
- 802 Marshall, J., Hill, C., Perelman, L., Adcroft., A., 1997b. Hydrostatic, quasi-  
 803 hydrostatic, and non-hydrostatic ocean modeling. *J. Geophys. Res.* 102,  
 804 5733–5752.
- 805 Marshall, J., Radko, T., 2003. Residual-mean solutions for the Antarctic  
 806 Circumpolar Current and its associated overturning circulation. *J. Phys.*  
 807 *Oceanogr.* 33, 2341–2354.

- Marshall, J., Shuckburgh, E., Jones, H., Hill, C., 2006. Estimates and implications of surface eddy diffusivity in the Southern Ocean derived from tracer transport. *J. Phys. Oceanogr.* 36, 1806–1821.
- Meijers, A. J., Bindoff, N. L., Roberts, J. L., 2007. On the total, mean, and eddy heat and freshwater transports in the southern hemisphere of a  $\frac{1}{8}^\circ \times \frac{1}{8}^\circ$  global ocean model. *J. Phys. Oceanogr.* 37, 277–295.
- Meredith, M. P., Naveira Garabato, A. C., Hogg, A. M., Farneti, R., 2012. Sensitivity of the overturning circulation in the Southern Ocean to decadal changes in wind forcing. *J. Clim.* 25, 99–110, doi:10.1175/2011JCLI4204.1.
- Meredith, M. P., Woodworth, P. L., Chereskin, T. K., Marshall, D. P., Allison, L. C., Bigg, G. R., Donohue, K., Heywood, K. J., Hughes, C. W., Hibbert, A., Hogg, A. M., Johnson, H. L., King, B. A., Leach, H., Lenn, Y., Morales-Maqueda, M. A., Munday, D. R., Naveira-Garabato, A. C., Provost, C., Sprintall, J., 2011. Sustained monitoring of the Southern Ocean at Drake Passage: past achievements and future priorities. *Rev. Geophys.* 49, RG4005, doi:10.1029/2010RG000348.
- Morrison, A. K., Hogg, A. M., 2013. On the relationship between Southern Ocean overturning and ACC transport. *J. Phys. Oceanogr.* 43, 140–148.
- Munday, D. R., Johnson, H. L., Marshall, D. P., 2013. Eddy saturation of equilibrated circumpolar currents. *J. Phys. Oceanogr.* 43, 507–532, doi:10.1175/JPO-D-12-095.1.
- Munday, D. R., Johnson, H. L., Marshall, D. P., 2015. The role of ocean gateways in the dynamics and sensitivity to wind stress of the

- 831 early Antarctic Circumpolar Current. *Paleoceanography* 30, 284–302,  
832 doi:10.1002/2014PA002675.
- 833 Munday, D. R., Zhai, X., 2015. Sensitivity of Southern Ocean circulation to  
834 wind stress changes: Role of relative wind stress. *Ocean Modell.* 95, 15–24,  
835 doi:10.1016/j.ocemod.2015.08.004.
- 836 Munk, W. H., Palmén, E., 1951. Note on the dynamics of the Antarctic  
837 Circumpolar Current. *Tellus* 3, 53–55.
- 838 Nadeau, L. P., Straub, D. N., 2009. Basin and channel contributions to a  
839 model Antarctic Circumpolar Current. *J. Phys. Oceanogr.* 39, 986–1002.
- 840 Nadeau, L. P., Straub, D. N., 2012. Influence of wind stress, wind stress curl,  
841 and bottom friction on the transport of a model Antarctic Circumpolar  
842 Current. *J. Phys. Oceanogr.* 42, 207–222.
- 843 Naveira Garabato, A. C., Jullion, L., Stevens, D. P., Heywood, K. J.,  
844 King, B. A., 2009. Variability of Subantarctic Mode Water and  
845 Antarctic Intermediate Water in the Drake Passage during the late-  
846 twentieth and early-twenty-first centuries. *J. Clim.* 22, 3661–3688,  
847 doi:10.1175/2009JCLI2621.1.
- 848 Rath, W., Greatbatch, R. J., Zhai, X., 2014. On the spatial and temporal  
849 distribution of near-inertial energy in the Southern Ocean. *J. Geophys.*  
850 *Res.* 119, 359–376, doi:10.1002/2013JC009246.
- 851 Roquet, F., 2013. Dynamical potential energy: A new approach to ocean  
852 energetics. *J. Phys. Oceanogr.* 43, 457–476, doi: 10.1175/JPO-D-12-098.1.



- 853 Saenz, J. A., Hogg, A. M., Hughes, G. O., Griffiths, R. W., 2012. Mechanical  
854 power input from buoyancy and wind to the circulation in an ocean model.  
855 *Geophys. Res. Lett.* 39, L13605, doi:10.1029/2012GL052035.
- 856 Shu, Q., Qiao, F., Song, Z., Xia, C., Yang, Y., 2011. Improvement of MOM4  
857 by including surface wave-induced vertical mixing. *Ocean Modell.* 40, 42–  
858 51.
- 859 Sinha, A., Abernathey, R. P., 2016. Time scale of Southern Ocean eddy  
860 equilibration. *J. Phys. Oceanogr.* 46, 2785–2805, doi:10.1175/JPO-D-16-  
861 0041.1.
- 862 Tailleux, R., 2009. On the energetics of stratified turbulent mixing, irre-  
863 versible thermodynamics, Boussinesq models and the ocean heat engine  
864 controversy. *J. Fluid Mech.* 638, 339–382.
- 865 Tailleux, R., 2013. Available potential energy and exergy in stratified flu-  
866 ids. *Annu. Rev. Fluid Mech.* 45, 35–58, doi:10.1146/annurev-fluid-011212-  
867 140620.
- 868 Tansley, C. E., Marshall, D. P., 2001. On the dynamics of wind-driven cir-  
869 cumpolar currents. *J. Phys. Oceanogr.* 31, 3258–3273.
- 870 Thomas, L. N., 2005. Destruction of potential vorticity by winds. *J. Phys.*  
871 *Oceanogr.* 35, 2457–2466.
- 872 Viebahn, J., Eden, C., 2010. Towards the impact of eddies on the response  
873 of the Southern Ocean to climate change. *Ocean Modell.* 34, 150–165.

- Winters, K. B., Lombard, P. L., Riley, J. J., D'Asaro, E. A., 1995. Available  
potential energy and mixing in density-stratified fluids. *J. Fluid Mech.* 289,  
115–128.
- Wunsch, C., 1998. The work done by the wind on the oceanic general circula-  
tion. *J. Phys. Oceanogr.* 28, 2332–2340.
- Wunsch, C., Ferrari, R., 2004. Vertical mixing, energy, and the general cir-  
culation of the oceans. *Annu. Rev. Fluid Mech.* 36, 281–314.
- Zhai, X., 2013. On the wind mechanical forcing of the ocean general circula-  
tion. *J. Geophys. Res.* 118 (1-17, doi:10.1002/2013JC009086).
- Zhai, X., Greatbatch, R. J., Eden, C., Hibiya, T., 2009. On the loss of wind-  
induced near-inertial energy to turbulent mixing in the upper ocean. *J.*  
*Phys. Oceanogr.* 39, 3040–3045.
- Zhai, X., Munday, D. R., 2014. Sensitivity of Southern Ocean overturning to  
wind stress changes: Role of surface restoring time scales. *Ocean Modell.*  
84, 12–25, doi:10.1016/j.ocemod.2014.09.004.

889 **List of Figures**

890	1	Atmospheric wind from the NCEP reanalysis (Kalnay et al.,	
891		1996). (a) Mean zonal wind at 10m (blue) and square root	
892		of atmospheric EKE (red). (b) Mean wind zonal wind stress	
893		(blue) and wind stress from the mean zonal wind (red) calcu-	
894		lated using the bulk formula of Large and Pond (1981). . . . .	43
895	2	Schematic of the model domain. The dashes at the surface	
896		mark where the heat flux is zero, with blue arrows showing	
897		regions of cooling and red arrows regions of heating. The grey	
898		shading near the northern boundary is the northern sponge.	
899		The symbols above the flux arrows show the wind forcing. The	
900		dashed lines schematically show the shape of the time-mean	
901		isotherms/isopycnals. . . . .	44
902	3	Model forcing as described in the text. (a) Northern bound-	
903		ary temperature restoring profile, (b) surface heat flux (posi-	
904		tive into ocean), (c) atmospheric wind profile with grey shad-	
905		ing showing one standard deviation about the mean for $\sigma_\tau =$	
906		$9\text{ms}^{-1}$ , (d) corresponding surface wind stress. . . . .	45
907	4	Variation in peak mean wind stress as the standard deviation	
908		of the atmospheric wind is varied. The peak mean wind stress	
909		of the control experiments is highlighted with a hexagram. . .	46
910	5	RMOC (in Sverdrups) at the control wind stress for (a) stochas-	
911		tic wind stress and (b) equivalent wind stress. Black contours	
912		are the zonal-time-average potential temperature ( $^{\circ}\text{C}$ ) and the	
913		colours are the RMOC with red indicating clockwise flow. The	
914		grey contour is the mixed layer depth from KPP, defined as	
915		the depth at which the water is $0.8^{\circ}\text{C}$ colder than the surface,	
916		see, e.g., Kara et al. (2000), for details. . . . .	47
917	6	Sensitivity to wind stress changes of energy budget diagnos-	
918		tics. (a) Power input vs. maximum wind stress and (b) bottom	
919		EKE dissipation vs. power input. The thin black in line in	
920		(b) has a gradient of 1 and highlight the departure from the	
921		simple relationship of Eq. (8). The control experiments are	
922		highlighted with hexagrams. . . . .	48

923	7	Domain average (a) viscosity and (b) temperature diffusivity	
924		as provided by the KPP parameterisation versus the maximum	
925		wind stress. The control experiments are highlighted with	
926		hexagrams. . . . .	49
927	8	Bar charts of the power budget for the control and extreme	
928		wind stress case for both stochastic and equivalent wind stress	
929		experiments. Presented as (a) absolute magnitude of the terms	
930		(b) relative to the total power input from the wind of each	
931		individual experiment. . . . .	50
932	9	Contours of time and zonal average potential temperature,	
933		every 0.5°C starting at 0.5°C, for paired stochastic (blue) and	
934		equivalent (red) wind stress experiments. (a) Control wind	
935		stress, with $\sigma_\tau = 9\text{ms}^{-1}$ , for the stochastic experiment. (b)	
936		Extreme wind stress, with $\sigma_\tau = 21\text{ms}^{-1}$ , for the stochastic	
937		experiment. . . . .	51
938	10	“Baroclinic” transport, as per $T_{tw}$ vs. maximum wind stress.	
939		The control experiments are highlighted with hexagrams. . . .	52
940	11	Sensitivity of the RMOC to changing wind stress across all	
941		experiments. Maximum Eulerian overturning in the domain	
942		( $\Psi_{\text{max}}$ , black dots) and maximum/minimum ( $\Psi_{\text{upper}}/\Psi_{\text{lower}}$ ,	
943		round/square) RMOC 100km south of the northern restoring	
944		zone and below 500m for the stochastic/equivalent wind	
945		stress experiments (blue/red). The control experiments are	
946		highlighted with hexagrams. . . . .	53
947	12	Quantitative tests of residual mean relationship between changes	
948		in eddy diffusivity and isopycnal slope. (a) Excluding any	
949		MOC changes, as per Eq. (21), (b) full relationship as per Eq.	
950		(20) including wind stress and MOC changes. The difference	
951		is taken between the equivalent and stochastic wind stress ex-	
952		periments with the equivalent wind stress experiment of each	
953		pair used as the initial state. The dotted lines cross at the	
954		origin and the solid line has a gradient of 1. . . . .	54

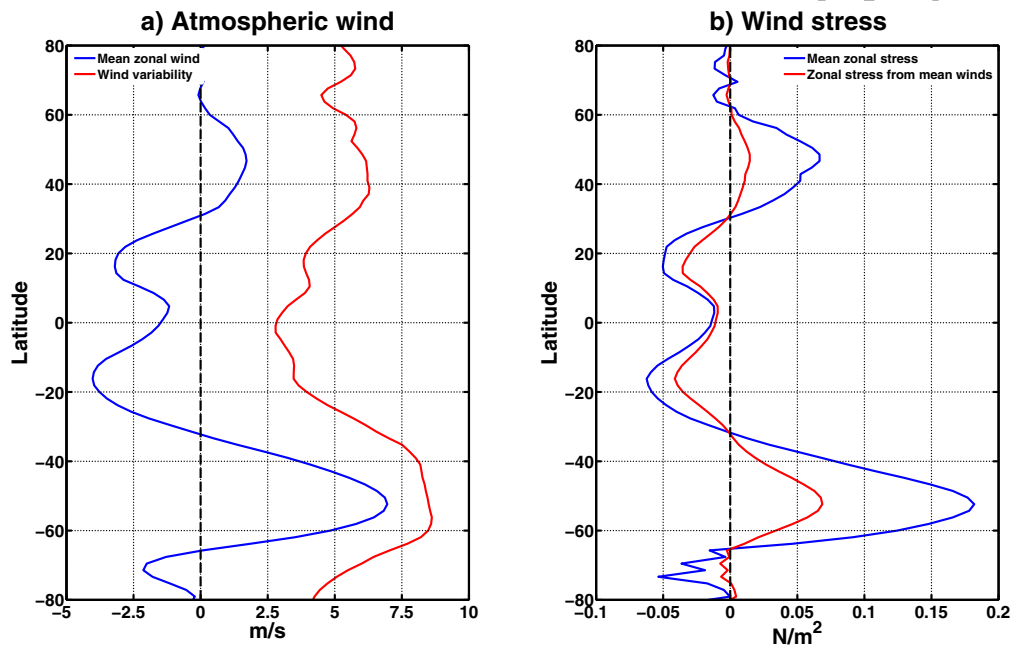


Figure 1: Atmospheric wind from the NCEP reanalysis (Kalnay et al., 1996). (a) Mean zonal wind at 10m (blue) and square root of atmospheric EKE (red). (b) Mean wind zonal wind stress (blue) and wind stress from the mean zonal wind (red) calculated using the bulk formula of Large and Pond (1981).

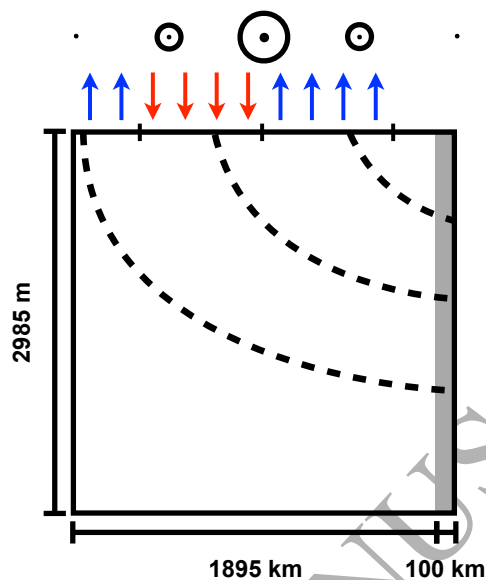


Figure 2: Schematic of the model domain. The dashes at the surface mark where the heat flux is zero, with blue arrows showing regions of cooling and red arrows regions of heating. The grey shading near the northern boundary is the northern sponge. The symbols above the flux arrows show the wind forcing. The dashed lines schematically show the shape of the time-mean isotherms/isopycnals.

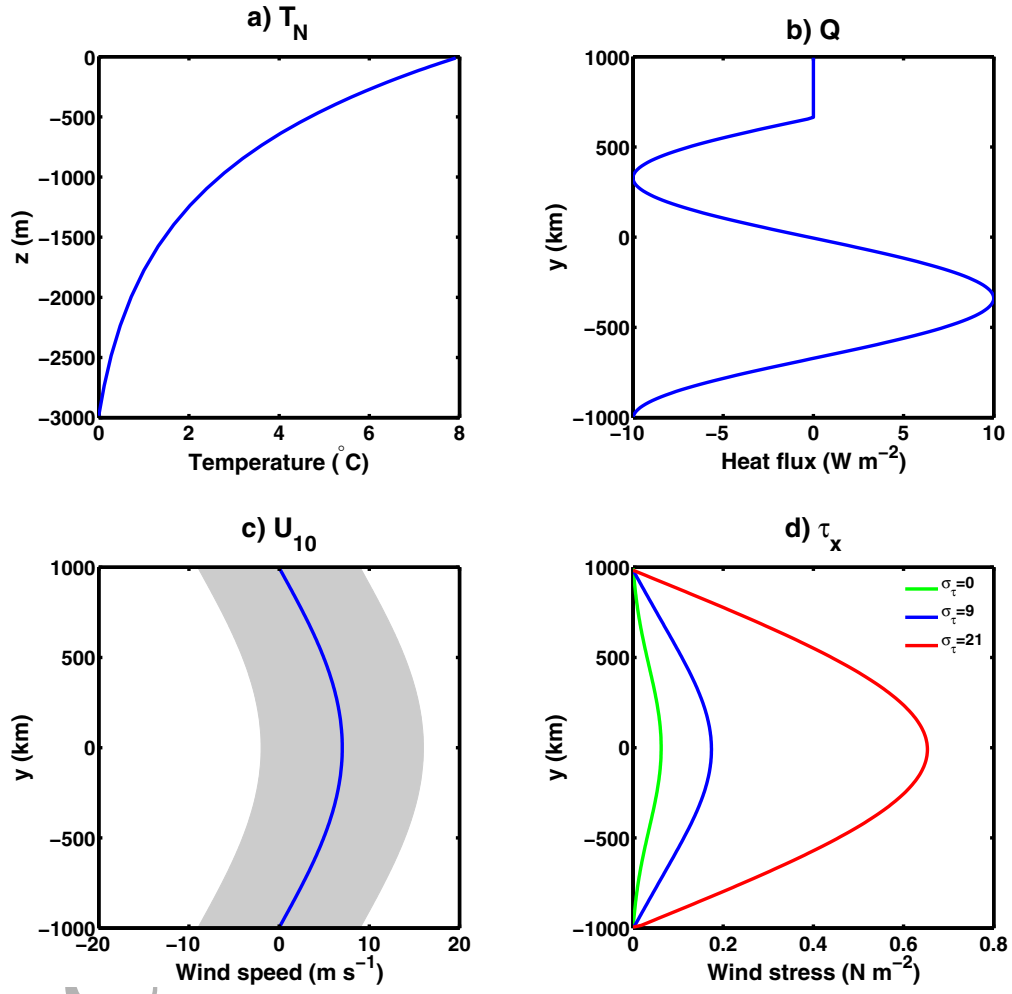


Figure 3: Model forcing as described in the text. (a) Northern boundary temperature restoring profile, (b) surface heat flux (positive into ocean), (c) atmospheric wind profile with grey shading showing one standard deviation about the mean for  $\sigma_{\tau} = 9 \text{ m s}^{-1}$ , (d) corresponding surface wind stress.

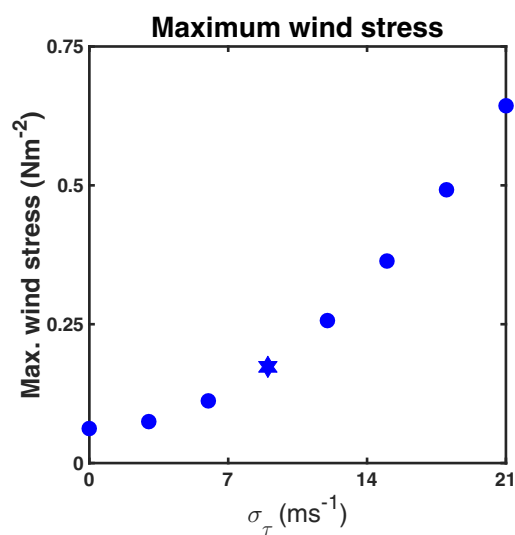


Figure 4: Variation in peak mean wind stress as the standard deviation of the atmospheric wind is varied. The peak mean wind stress of the control experiments is highlighted with a hexagram.



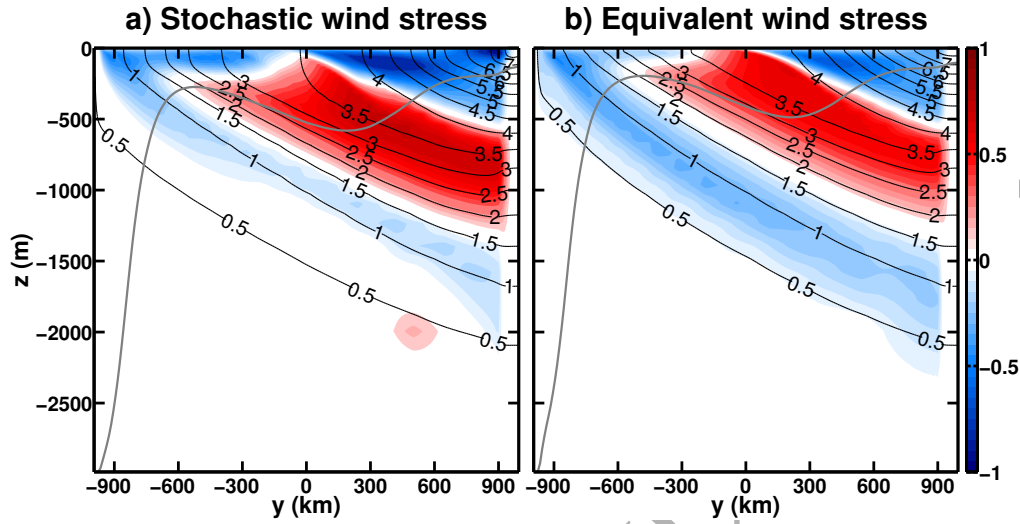


Figure 5: RMO (in Sverdrups) at the control wind stress for (a) stochastic wind stress and (b) equivalent wind stress. Black contours are the zonal-time-average potential temperature ( $^{\circ}\text{C}$ ) and the colours are the RMO with red indicating clockwise flow. The grey contour is the mixed layer depth from KPP, defined as the depth at which the water is  $0.8^{\circ}\text{C}$  colder than the surface, see, e.g., Kara et al. (2000), for details.

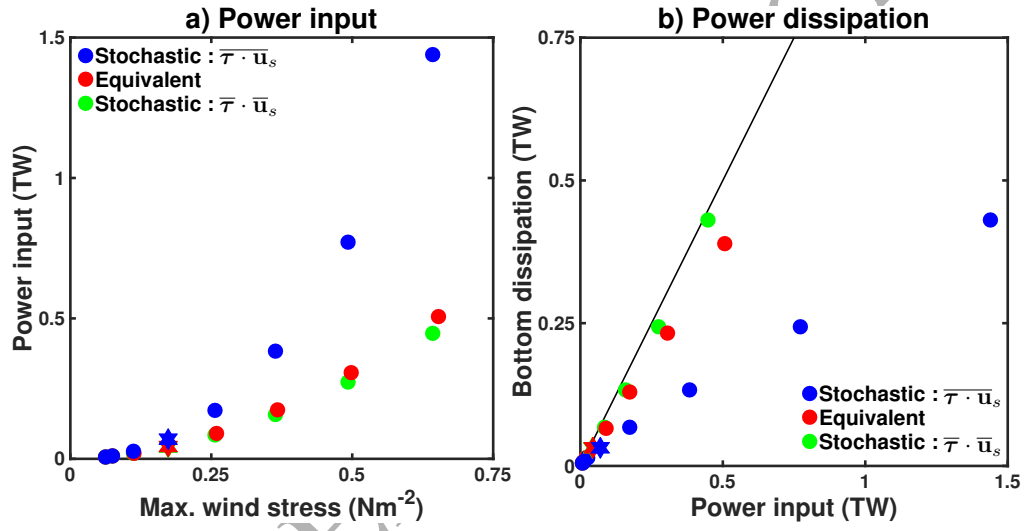


Figure 6: Sensitivity to wind stress changes of energy budget diagnostics. (a) Power input vs. maximum wind stress and (b) bottom EKE dissipation vs. power input. The thin black line in (b) has a gradient of 1 and highlights the departure from the simple relationship of Eq. (8). The control experiments are highlighted with hexagrams.

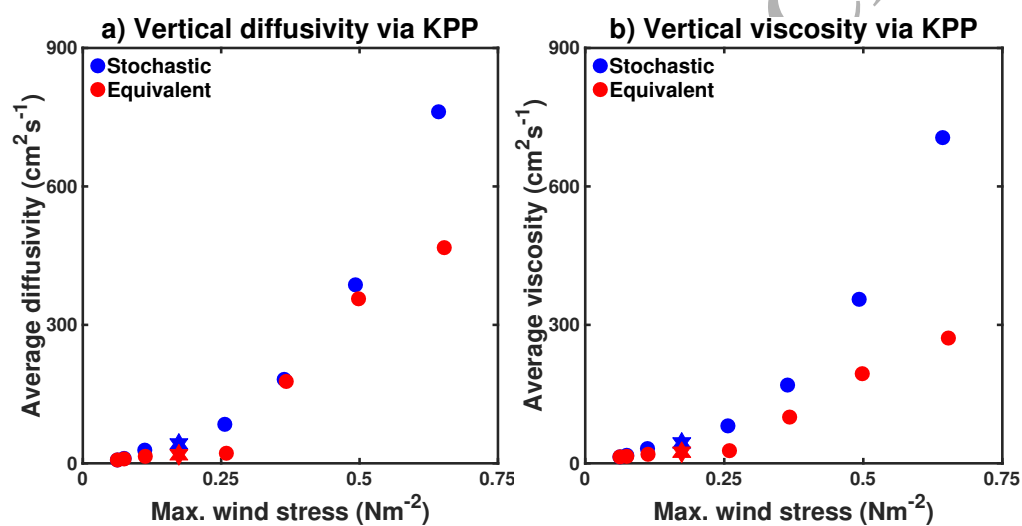


Figure 7: Domain average (a) viscosity and (b) temperature diffusivity as provided by the KPP parameterisation versus the maximum wind stress. The control experiments are highlighted with hexagrams.

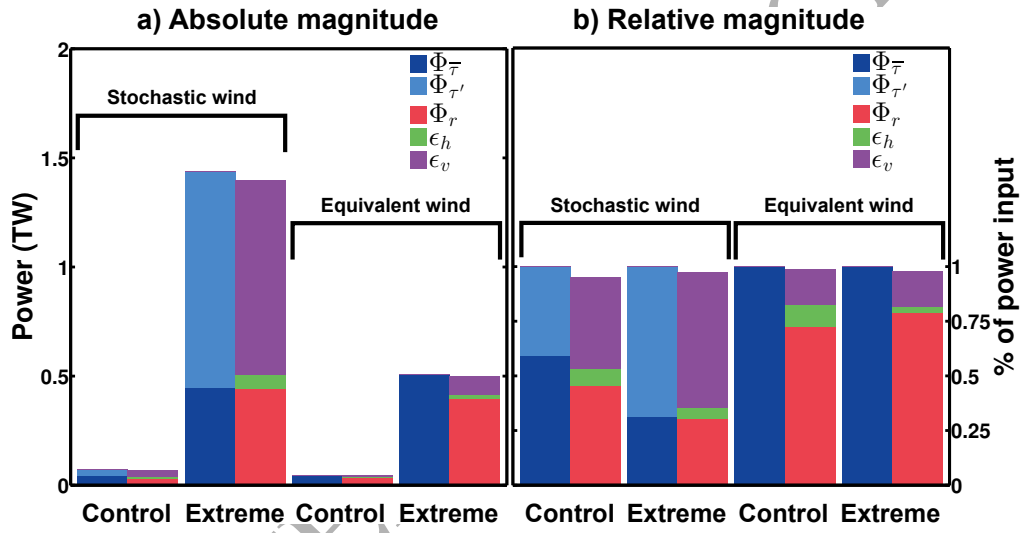


Figure 8: Bar charts of the power budget for the control and extreme wind stress case for both stochastic and equivalent wind stress experiments. Presented as (a) absolute magnitude of the terms (b) relative to the total power input from the wind of each individual experiment.

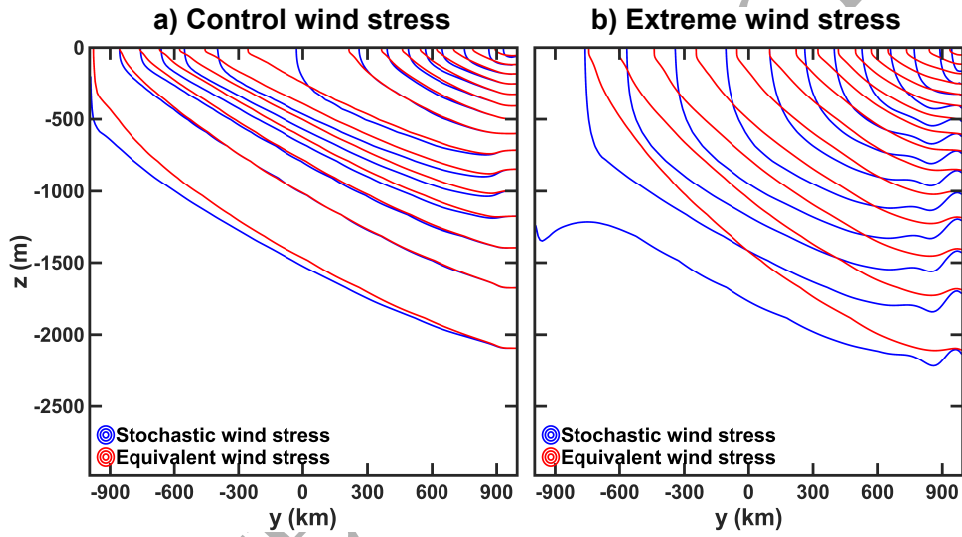


Figure 9: Contours of time and zonal average potential temperature, every  $0.5^{\circ}\text{C}$  starting at  $0.5^{\circ}\text{C}$ , for paired stochastic (blue) and equivalent (red) wind stress experiments. (a) Control wind stress, with  $\sigma_{\tau} = 9\text{ms}^{-1}$ , for the stochastic experiment. (b) Extreme wind stress, with  $\sigma_{\tau} = 21\text{ms}^{-1}$ , for the stochastic experiment.

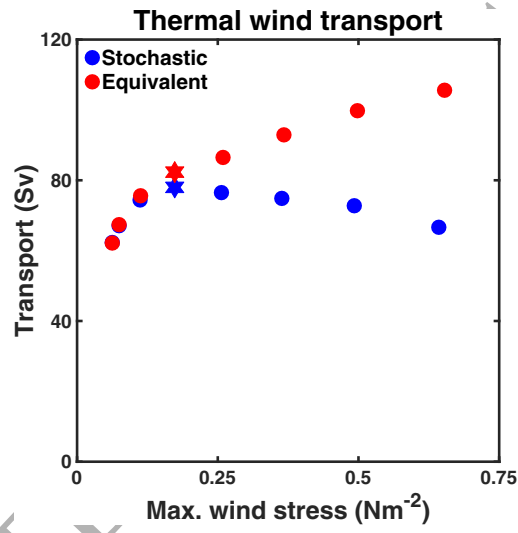


Figure 10: “Baroclinic” transport, as per  $T_{tw}$  vs. maximum wind stress. The control experiments are highlighted with hexagrams.

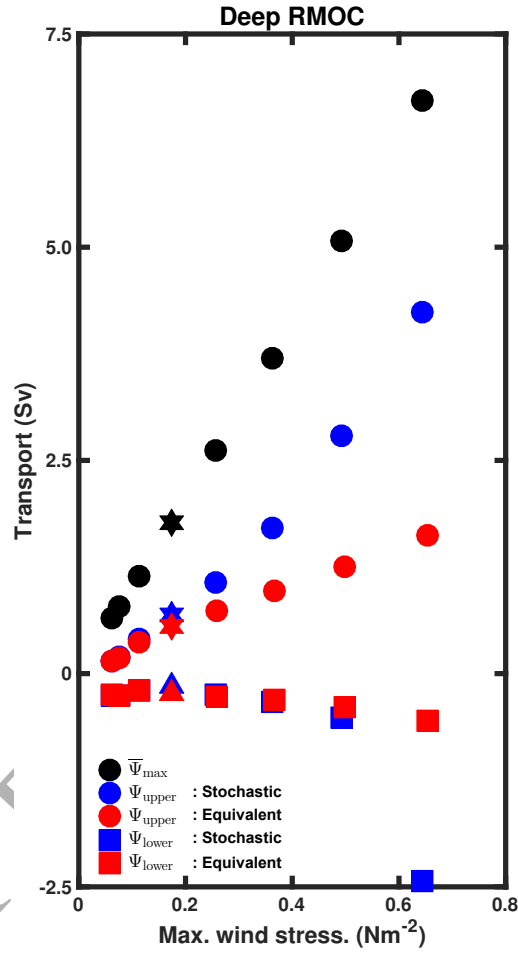


Figure 11: Sensitivity of the RMOC to changing wind stress across all experiments. Maximum Eulerian overturning in the domain ( $\bar{\Psi}_{\max}$ , black dots) and maximum/minimum ( $\Psi_{\text{upper}}/\Psi_{\text{lower}}$ , round/square) RMOC 100km south of the northern restoring zone and below 500m for the stochastic/equivalent wind stress experiments (blue/red). The control experiments are highlighted with hexagrams.

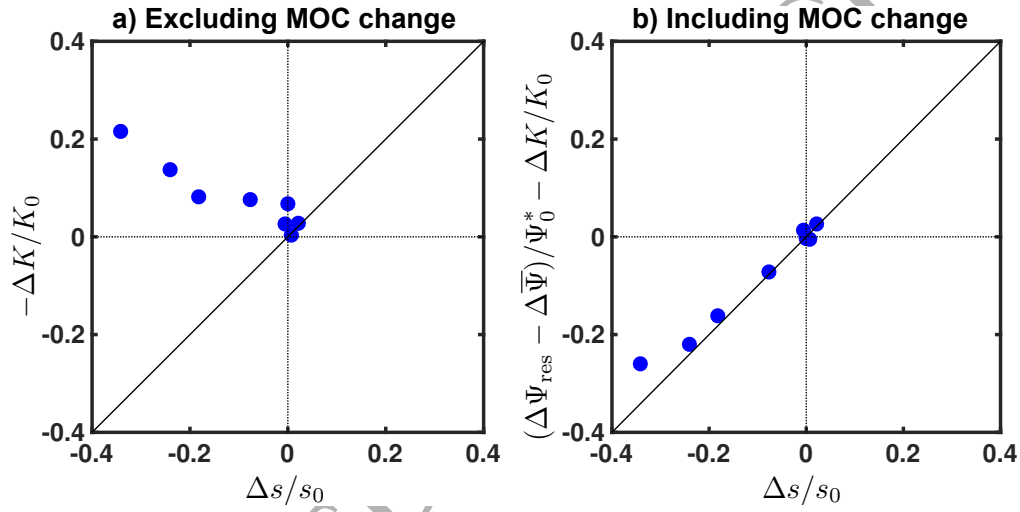


Figure 12: Quantitative tests of residual mean relationship between changes in eddy diffusivity and isopycnal slope. (a) Excluding any MOC changes, as per Eq. (21), (b) full relationship as per Eq. (20) including wind stress and MOC changes. The difference is taken between the equivalent and stochastic wind stress experiments with the equivalent wind stress experiment of each pair used as the initial state. The dotted lines cross at the origin and the solid line has a gradient of 1.



955 **List of Tables**

956	1	Model Parameters . . . . .	56
957	2	Key diagnostics of the control experiments. Type of wind	
958		stress, Domain average EKE, Total circumpolar transport,	
959		Bottom transport, Thermal wind transport, $\Psi_{\text{upper}}$ , $\Psi_{\text{lower}}$ , do-	
960		main average viscosity/diffusivity from KPP ( $A/K$ ). . . . .	57

Table 1: Model Parameters

Parameter	Symbol	Value	Units
Domain size	$L_x, L_y$	1000, 1990	km
Latitude of sponge edge	$L_{sponge}$	1890	km
Domain depth	$H$	2985	m
Boussinesq reference density	$\rho_0$	1000	$\text{kg m}^{-3}$
Thermal expansion coefficient	$\alpha$	$2 \times 10^{-4}$	$\text{K}^{-1}$
Coriolis parameter	$f_0$	$-1 \times 10^{-4}$	$\text{km s}^{-1}$
Gradient in Coriolis parameter	$\beta$	$1 \times 10^{-11}$	$\text{m}^{-1} \text{s}^{-1}$
Surface heat flux magnitude	$Q_0$	10	$\text{W m}^{-2}$
Peak wind speed	$U_0$	7	$\text{m s}^{-1}$
Bottom drag coefficient	$r_b$	$1.1 \times 10^{-3}$	$\text{m s}^{-1}$
Sponge restoring timescale	$t_{sponge}$	7	days
Sponge vertical scale	$h_e$	1000	m
Horizontal grid spacing	$\Delta x, \Delta y$	10	km
Vertical grid spacing	$\Delta z$	10-250	m
Vertical diffusivity ( $\theta$ )	$\kappa_v$	$10^{-5}$	$\text{m}^2 \text{s}^{-1}$
Horizontal diffusivity ( $\theta$ )	$\kappa_h$	0	$\text{m}^4 \text{s}^{-1}$
Vertical viscosity (momentum)	$A_v$	$10^{-3}$	$\text{m}^2 \text{s}^{-1}$
Horizontal hyperviscosity	$A_4$	$10^{10}$	$\text{m}^4 \text{s}^{-1}$

Table 2: Key diagnostics of the control experiments. Type of wind stress, Domain average EKE, Total circumpolar transport, Bottom transport, Thermal wind transport,  $\Psi_{\text{upper}}$ ,  $\Psi_{\text{lower}}$ , domain average viscosity/diffusivity from KPP ( $A/K$ ).

Experiment	EKE ( $\text{cm}^2\text{s}^{-2}$ )	$T_{ACC}$ (Sv)	$T_b$ (Sv)	$T_{tw}$ (Sv)	$\Psi_{\text{upper}}$ (Sv)	$\Psi_{\text{lower}}$ (Sv)	$A/K$ ( $\text{cm}^2\text{s}^{-1}$ )
Stochastic	54	621	543	78	0.69	-0.15	45/42
Equivalent	49	630	548	82	0.55	-0.23	24/18